Comparative Study of Zinc Cold Spray Coating and Pre-Treatments for Magnesium Alloys

Sridhar Niverty[1], Mayur Pole[1], Jijo Christudasjustus[2], Jiheon Jun[3], James V Haag[1], Tanvi A Ajantiwalay[1], Rajib Kalsar[1], Vineet V Joshi[1]

[1]Energy and Environment Directorate, Pacific Northwest National Laboratory, WA- 99354

[2]Physical and Computational Sciences Directorate, Pacific Northwest National Laboratory, WA- 99354

[3]Materials Science and Technology Division, Oak Ridge National Laboratory, TN- 37830

JOM Special Issue: Advanced Surface Processing of Mg Alloys for Engineering Applications

Abstract

Magnesium (Mg) alloys are appealing for automotive lightweighting owing to their high specific strength. However, their susceptibility to corrosion in harsh environments remains a major challenge. Conventional industrial pre-treatment coatings, including zinc phosphate, chromate conversion, and non-chromate conversion, often exhibit discontinuities and microcracks, leading to localized corrosion near fasteners and parting lines. This study investigates cold sprayed Zinc (Zn) coatings as a novel pre-treatment alternative for high-pressure die cast (HPDC) AZ91 Mg alloys, demonstrating significant improvements in wear and corrosion performance. Cold spray produces uniform and robust coatings, reducing wear rate by over 50% and reducing corrosion rate by over 99.3 % as measured by evolved hydrogen release, compared to traditional pre-treatments. Multimodal corrosion testing reveals that Zn cold spray coatings form a protective layer during exposure, minimizing general and filiform corrosion, and exhibiting corrosion potential (E_{corr}) that is nobler by ~400 mV than the surfaces of both pre-treated and uncoated AZ91. Scalability of cold spray for selective application around multimaterial joints further strengthens their industrial viability. This work establishes Zn cold spray coatings as highly effective pre-treatment solutions for the advancement of corrosion resistant Mg alloy components in automotive applications.

Keywords: Automotive Pre-treatment Coatings, Solid Phase Processing, Multimodal Corrosion, Wear Mechanism, Microscopy.

Highlights

- Zn cold spray coatings were compared with commonly used industrial pre-treatment coatings in terms of their wear and corrosion properties.
- Zn cold spray coatings show atleast a 50% lower wear rate and 99.3% lower corrosion rate (measured using evolved hydrogen gas measurements) as compared to pre-treatment coatings.
- During potentiodynamic polarization, the pre-treatments undergo a combination of localized pitting and filiform corrosion whereas the Zn cold spray coating forms a protective layer/patina that disintegrates only at very high applied potentials (greater than -400 mV vs SCE), indicating the protective ability of the layer. The Zn layer also exhibits an E_{corr} value that is ~400 mV (vs SCE) more noble than that of the other pretreatment coatings.
- Apart from the improved corrosion and mechanical properties, cold spray coatings of Zn also offer greater thickness control as compared to the current state-of-the-art pre-treatment coating methods and the ability to integrate into robotic systems for selective coating of Mg alloys around vulnerable areas of HPDC Mg alloy automotive components.

1. Introduction

Magnesium (Mg) alloys are excellent candidate structural materials for automotive lightweighting due to their high specific strength [1–3]. Mg alloys, specifically AZ91, is used to make several vehicle parts [1,4–6] such as wheels [7], central control bracket [8,9], transmission housing [10], inner panel [11], swivel plate [12], headlight bracket [10] and clutch housing [13] using casting methods such as sand casting, high pressure die casting (HPDC), squeeze casting and thixocasting. However, their implementation and long-term reliability is primarily limited by their poor corrosion resistance [14–21]. Corrosion susceptibility is markedly increased in automotive service environments where components experience prolonged high relative humidity, chloride exposure from road salts, and location-dependent temperature fluctuations throughout the year. Currently, a variety of coating systems have been reported, and some are utilized to cover and protect the surface of Mg alloys to prevent their exposure to the environment [22–27]. These coating systems are often composed of multiple layers, each with a specific role to play in protecting the surface. Figure 1 shows a schematic of the coatings that are generally utilized on the surface of Mg alloys. During the automotive coating process, the Mg alloys undergo a pre-treatment or anodizing coating operation that deposits a thin layer (~10 nm in anodizing up to 10 μm in pre-treatment conversion coatings) of pre-treatment coating on the surface. Pre-treatment conversion coatings on vehicle bodies fulfill three essential functions viz: (1) they provide enhanced corrosion protection compared to untreated metal surfaces, offering improvement in longevity and durability, (2) they facilitate stronger adhesion between the paint and the metal substrate, forming a more durable chemical bond than paint applied directly onto the bare Mg alloys and, (3) finally, conversion coatings modify the surface topography by creating a rough layer, which enhances the mechanical anchoring properties for subsequent paints and other organic coatings, further optimizing adhesion performance [28]. Following pre-treatment, an E-coat is applied as the next step, followed by a primer, basecoat, and clear coat top coating for visible surfaces requiring aesthetic quality (e.g., Mercedes-Benz SL/SLK series folding roofs). For surfaces that experience wear and are not visible (e.g., Ford Mustang Shelby GT500 strut tower braces), a powder coating is applied either with or without an E-coat and finished with a sealant depending on the specific protection requirements of the part [29]. The specific top coat system chosen is thus dependent on the surface's location and required properties, as exemplified in Figure 1(a) and 1(b), respectively [30].

Despite these multilayer strategies, recent work has revealed persistent deficiencies in the corrosion protection of coated Mg alloys. Specifically, the use of ceramic based pre-treatment coatings with a top coating layer of powder coat was observed to insufficiently protect a cast AE44 Mg alloy tower brace from corrosion in a salt fog environment [31]. While general corrosion and coating blistering were observed on the surface, the most vulnerable areas were regions adjacent to fasteners comprising dissimilar material

washers and bolts/rivets, and parting lines [31]. This indicates that the corrosive fluid is able to reach the Mg alloy substrate at locations of local discontinuity (due to friction, surface damage, or general wear and tear) in the coating and locally initiate localized corrosion. Thus, there is a strong need to design a coating for Mg alloys that is more resistant to wear and corrosion at vulnerable locations.

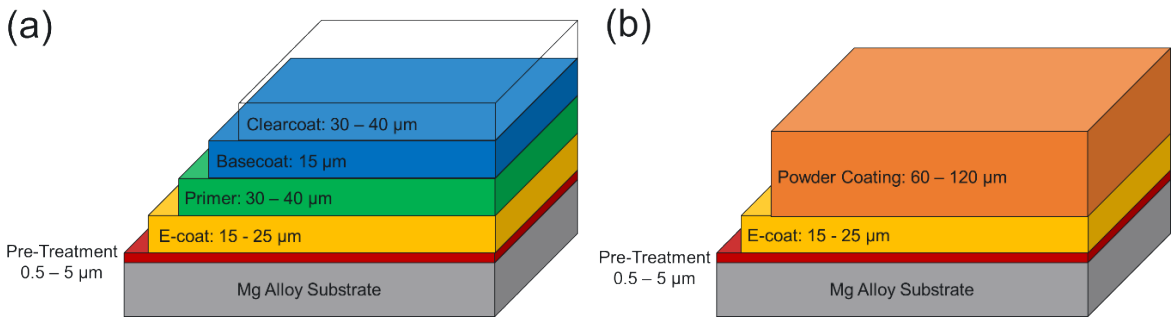

Figure 1: Schematic showing the various layers of coatings that are applied on Mg alloy parts in automotive applications, (a) Coating layers on visible Mg alloy surfaces, (b) Coating layers on non-visible Mg alloy surfaces.

Recently, the authors of this manuscript have demonstrated the benefit of using cold spray coatings to improve the surface properties of Mg alloy surfaces [32–35]. Cold spray is a solid phase coating method that enables the deposition of powders of the desired coating by ejecting them at supersonic velocities on to a substrate surface. The high velocity of powder deposition leads to the generation of significant localized pressure and heating, resulting in the development of a metallurgical bond at the particle-substrate interface or at particle-particle interfaces [36–40]. Using cold spray, the authors have demonstrated the ability to deposit pure Zn and AA6061 coatings [33,34]. These coatings improved the surface wear and corrosion resistance of the Mg alloy AZ91 while also offering the ability to precisely control deposition thickness and microstructural features such as porosity. Furthermore, cold spray offers unique scalability for selective reinforcement near fasteners, multimaterial joints, and regions historically prone to localized coating failure. These coatings also enable joining of the Mg alloys to galvanized steel surfaces (using Zn coated Mg) or joining to Al- alloy sheet material (using AA6061 coating) to either eliminate or minimize galvanic corrosion potential differences. Due to their ability to protect the surface from corrosion and precisely control deposition and properties, cold spray coatings can be an excellent choice as a pre-treatment to support the deposition of E-coat and top coats on them for localized corrosion and wear control in Mg alloys.

In this study, we investigated the microstructure, wear and corrosion performance of Zn cold sprayed and industrial pre-treated HPDC AZ91D. Three pre-treatments, namely zinc phosphate pre-treatment, chromate

conversion and non-chromate conversion pre-treatment coatings, were selected as industrial benchmarks. The benefits of using Zn cold sprayed AZ91 in terms of performance and scalability are discussed. The results establish that cold sprayed Zn provides uniform coating morphology and greatly improves resistance to localized corrosion and wear performance.

2. Methods

Uncoated and pre-treated HPDC AZ91 plates of dimensions- 101.6 mm x 152.4 mm x 3.048 mm (i.e., 4'' x 6" x 0.12") were obtained from ACT Test Panels LLC (Hillsdale, Michigan, USA). The widely used zinc phosphate, chromate conversion and non-chromate conversion pre-treatments were investigated in this study. Coupons were cut from these plates and prepared for imaging using scanning electron microscopy (SEM). Energy Dispersive Spectroscopy (EDS) was utilized to perform elemental analysis and map the distribution of elements within the coatings and at coating-substrate interfaces.

Uncoated AZ91 samples were cold spray coated using the optimized parameters as discussed in a previous manuscript by the authors [33]. Zn powders were obtained from Belmont Metals (Product code: 8024). The powders were sieved to be in a size range between 20 – 52 μm and dried at 120°C for 2 hours. The 20-52 microns range of powder particles were chosen after careful microstructural optimization as documented in [32,33]. During the optimization process, we found that including powders below 20 microns led to inadequate bonding between particles as we could not achieve the critical velocity needed for bonding. This led to high interconnected porosity % and sections of the coating easily flaking off of the bulk of the coating during sample preparation or adhesion testing. Similarly, particles larger than 52 microns showed poor deposition due to significant erosion that is attributable to their large size and high kinetic energy transfer into the substrate or coating upon impact. Using a range of 20-52 microns yielded dense coating microstructures devoid of interconnected porosity. A nitrogen carrier gas pressure of 3.5 MPa, gas temperature of 400°C, standoff distance of 25.4 mm, overlap distance of 0.5 mm and traverse speed of 200 mm/s were utilized to coat pure Zn powders on to AZ91 using a VRC Metal Systems Gen III High-Pressure Cold Spray System. Further details regarding the optimization process of cold spray parameters can be found in [33]. Cold spray coatings were deposited with 1 pass sprayed at 45 degree spray angle primarily to clean the surface and 2 passes sprayed at a 90 degree spray angle (normal to the surface). This resulted in coatings with a thickness of ~500 ± 30 μm.

2.1 SEM and EDS characterization

One sample from each pre-treatment coating was imaged in the cross-section using the JOEL JSM IT500 HR SEM at 5kV accelerating voltage, probe current (PC) 75 using an objective aperture of size 40 μm. The backscatter electron (BSE) images were each collected at 7500X magnification and later stitched together

into a montage. The thickness of the cold spray coatings was measured and validated using two methods- (i) Using a laser based topography measurements that measured height of the sample before cold spray and after cold spray, and (ii) using images of the cross section of the cold sprayed samples obtained using SEM. The thickness of the coating was measured at several areas of the sample and an average of atleast 5 areas was taken. The thickness of the industrial pre-treatments were measured from images of the cross section obtained using SEM.

To analyze the chemistry of the coatings, energy dispersive X-ray spectroscopy (EDS) scans were performed at 10,000X magnification at the coating/substrate interface. EDS maps were collected at 20kV voltage, PC75 and a 100 µm sized objective aperture. Each individual map was collected by scanning at least three frames at 5 µs dwell time and a pixel resolution of 2048. For SEM and EDS micrographs from the Zn cold spray coated AZ91 sample, the reader is referred to reference [33].

2.2 Grazing incidence X-ray diffraction

GI-XRD measurements were performed using a Rigaku SmartLab diffractometer equipped with a rotating Cu anode source operating at 45 kV and 200 mA. The incident Cu Kα radiation ($\lambda = 1.5406$ Å) was filtered using a two-bounce Ge (220) monochromator. Diffracted intensities were collected using a HyPix-3000 2D hybrid pixel detector operated in 0D point detection mode for out-of-plane scans. Data were acquired over a 2θ range of 10-100° with a step size of 0.02° and a scan rate of 0.5° $2\theta \cdot min^{-1}$. A grazing incidence geometry was used to enhance surface sensitivity and minimize the contribution from the bulk substrate, enabling detection of thin surface coatings and conversion layers.

2.3 Wear and Hardness Testing

Tribological tests were conducted on the 25.4 mm x 25.4 mm (1" x 1") pretreated AZ91D coupons and compared with bare AZ91 and cold-sprayed Zn coatings. A pin-on-disk tribometer (Anton Paar) was used to perform the wear experiments in accordance with ASTM G133. A 6.35 mm-diameter tungsten carbide (WC–Co) ball served as the counterface. Tests were carried out under a normal load of 1 N, corresponding to a maximum Hertzian contact pressure of approximately 350 MPa and a maximum shear stress of ~105 MPa values exceeding the yield strengths of both AZ91 (~150 MPa) and Zn (~90 MPa). Each test consisted of 5000 sliding cycles at a frequency of 5 Hz, producing a total sliding distance of 120 m with a 6 mm stroke length, selected to ensure evaluation of the steady-state friction regime. Three replicates were performed for each material condition, and all experiments were conducted under ambient laboratory air. The coefficient of friction (COF) was recorded using Tribo 1.4x software. Post-test wear tracks were examined using a Keyence white-light interferometer, and 3D topographical profiles were acquired to quantify wear widths, wear depths, and wear volume loss (mm^3) using VR-5000 series analysis software.

Wear rates ($mm^3/N \cdot m$) were subsequently determined by normalizing the measured wear volume by the applied load and total sliding distance. Finally, Vickers microhardness of the coatings was systematically measured at ambient conditions using a Model FM-ARS9000 fully automated Vickers microhardness testing system. Indentations were performed under a constant load of 200 gf with a dwell time of 12 s. To minimize potential interactions between adjacent plastic deformation zones and ensure statistical reliability, successive indents were spaced 0.250 mm apart along both the x- and y-directions, in compliance with ASTM E384 guidelines [41].

2.4 Corrosion Testing

2.4.1 Multimodal Corrosion Measurement

Multimodal electrochemical testing was utilized to investigate the corrosion performance of the pre-treatment coatings and the Zn cold spray coating under accelerated corrosion. A PNNL-developed multimodal corrosion measurement system that can perform electrochemical testing and sample imaging simultaneously, was utilized to correlate the electrochemical data with ongoing microstructural evolution during corrosion [42]. Open circuit potential (OCP) was monitored for a duration of 1800 seconds following which potentiodynamic polarization (PD) was performed from -0.2 V below the measured OCP value, until 0 V (vs SCE). A scan rate of 10 mV/minute was utilized to polarize the samples with a saturated calomel electrode (SCE) as reference and two graphite rods as counter electrodes in 3.5 wt.% NaCl solution. The PD curves were fitted to the Butler-Volmer equation using the Gamry Analyst software package. The fitting range was limited to the quasi-linear portions of the anodic and cathodic polarization branches around E_{corr} to ensure validity of the Tafel approximation. Corrosion parameters such as corrosion potential- E_{corr} (mV), corrosion current- I_{corr} (A/cm^2), anodic slope- βa (V/decade), cathodic slope- βc (V/decade) and corrosion rate (mpy) were obtained. The Tafel fit results were compared with results from manual fitting and a deviation of less than 15% was considered acceptable. A chi-squared fit value of less than 1.0 was considered acceptable for results obtained from Tafel fitting. Results from manual fitting were used instead of Tafel fit results in samples that exhibited chi-squared values greater than 1.0.

The Polarization Resistance-Rp ($\Omega.cm^2$) was calculated using the Stern-Geary relationship [43]:

$$R_p = \frac{\beta_a \beta_c}{2.303\, I_{corr}(\beta_a + \beta_c)}$$

where βa and βc are expressed in V/decade and I_{corr} in A/cm^2.

A Tokina atx-i macrolens and a Basler Ace camera were utilized to perform high resolution imaging of the sample surface during the corrosion process. Images were obtained at regular intervals of 5 seconds per

frame for the full duration of the OCP and PD measurements, compiled together into an image stack and correlated with the electrochemical data. ImageJ was utilized to crop the images acquired during corrosion, insert scale bars and to compile the imaging data [44]. A comparison was made between the surface corrosion behavior, OCP and PD behaviors of the pre-treatment and Zn cold sprayed samples.

2.4.2 Hydrogen Collection

Hydrogen (H_2) collection was performed for Zn cold sprayed and three pretreated HPDC AZ91D samples to evaluate the cumulative amount of Mg anodic dissolution over time in 3.5 wt.% NaCl solution. The coated/treated AZ91D samples were masked to expose a circular area with Ø = 10.3 mm (i.e. 0.833 cm^2) and immersed in ~3 L of NaCl solution reservoir. An inverted funnel was placed right above the exposed area of the samples to collect H_2 generated. The H_2 volumes were periodically recorded, and the volume data were converted to Mg corrosion rates in mm per year unit.

3. Results

3.1 Microstructural characterization of pre-treatment coated AZ91

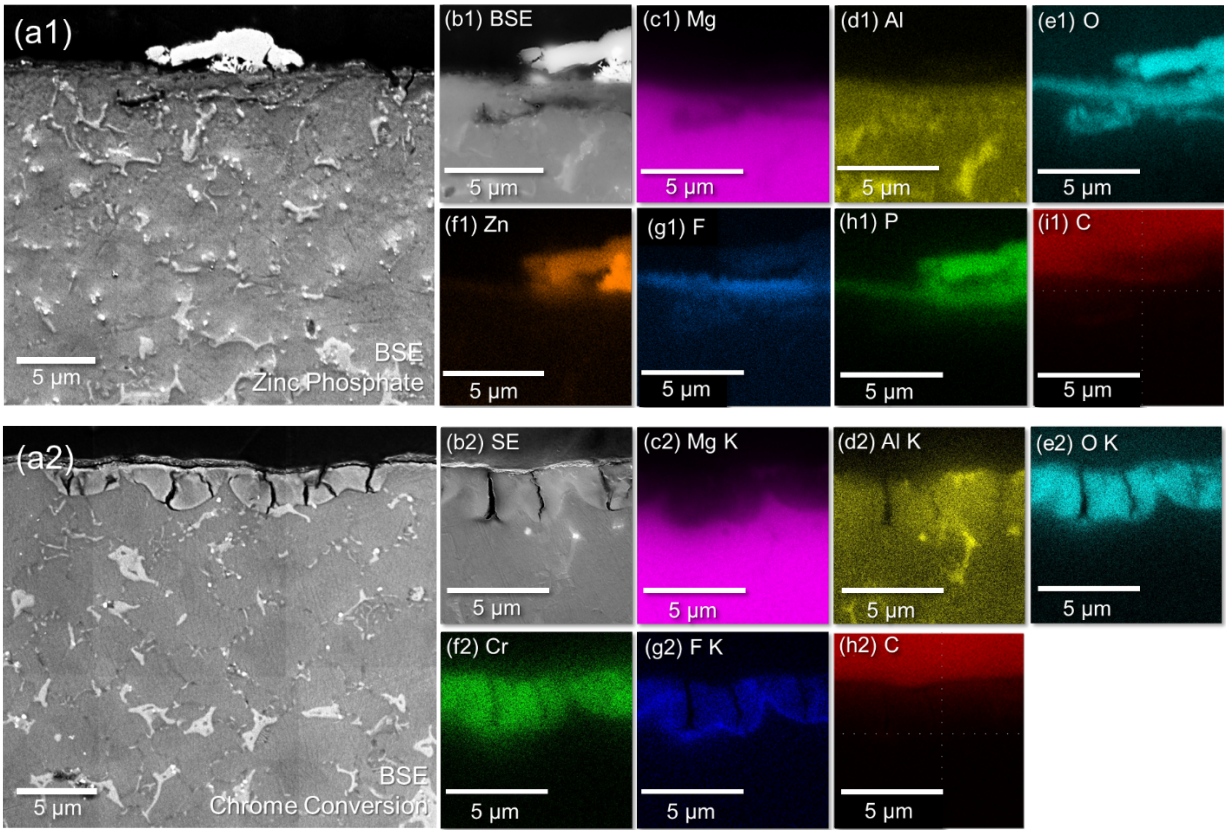

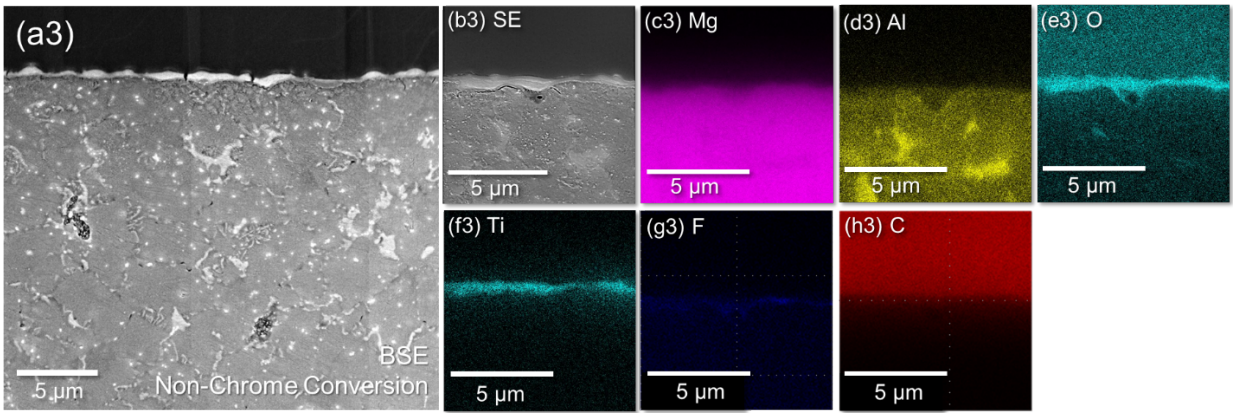

Figure 2: SEM-BSE montage of cross-sections of pre-treatment coatings on HPDC AZ91 substrates: (a1) Zinc phosphate coating (a2) Chromate conversion coating, (a3) Non-Chromate conversion coating, and corresponding EDS maps showing individual elemental composition for (b1-i1) zinc phosphate, (b2-h2) chromate conversion, and (b3-h3) non-chromate conversion coatings, respectively.

Figure 2 shows the detailed microstructure along with the chemical composition at the coating/substrate interface for the three pre-treatments obtained using SEM and EDS. SEM images show the morphology of the pre-treatment coatings on top of the HPDC AZ91 substrates. The AZ91 substrates showed the presence of bright particles composed of constituent $Mg_{17}Al_{12}$ in a cast Mg-rich alloy matrix. The coatings were observed to range from 0.5 – 5 µm in thickness. EDS was performed to identify the primary chemical species in these coatings, and a further detailed assessment of the coatings is needed to identify all trace species in these industrial coatings and quantify their approximate compositions. In case of the zinc phosphate shown in Figure 2(a1)-(i1), broken clusters of the coating comprising zinc (Zn), phosphorous (P) and oxygen (O) were observed on the AZ91 substrate suggesting that the coating was discontinuous. For the chromate conversion (a2-h2), a very discontinuous coating layer was observed along with several micro-cracks. EDS spectra confirm the presence of chromium (Cr) and oxygen (O); however, a notable fluorine (F) signal was also obtained. In both cases, no significant intermixing with the substrate was observed. For the non-chromate conversion coatings, a sub-micron thin layer of titanium (Ti) was seen along with significant oxygen (O) presence at the interface. Similar to the chromate conversion coating, several micro-cracks were seen in the Ti layer. The chemical composition of the coatings is further examined using a grazing angle X-ray diffraction technique as discussed in the next section.

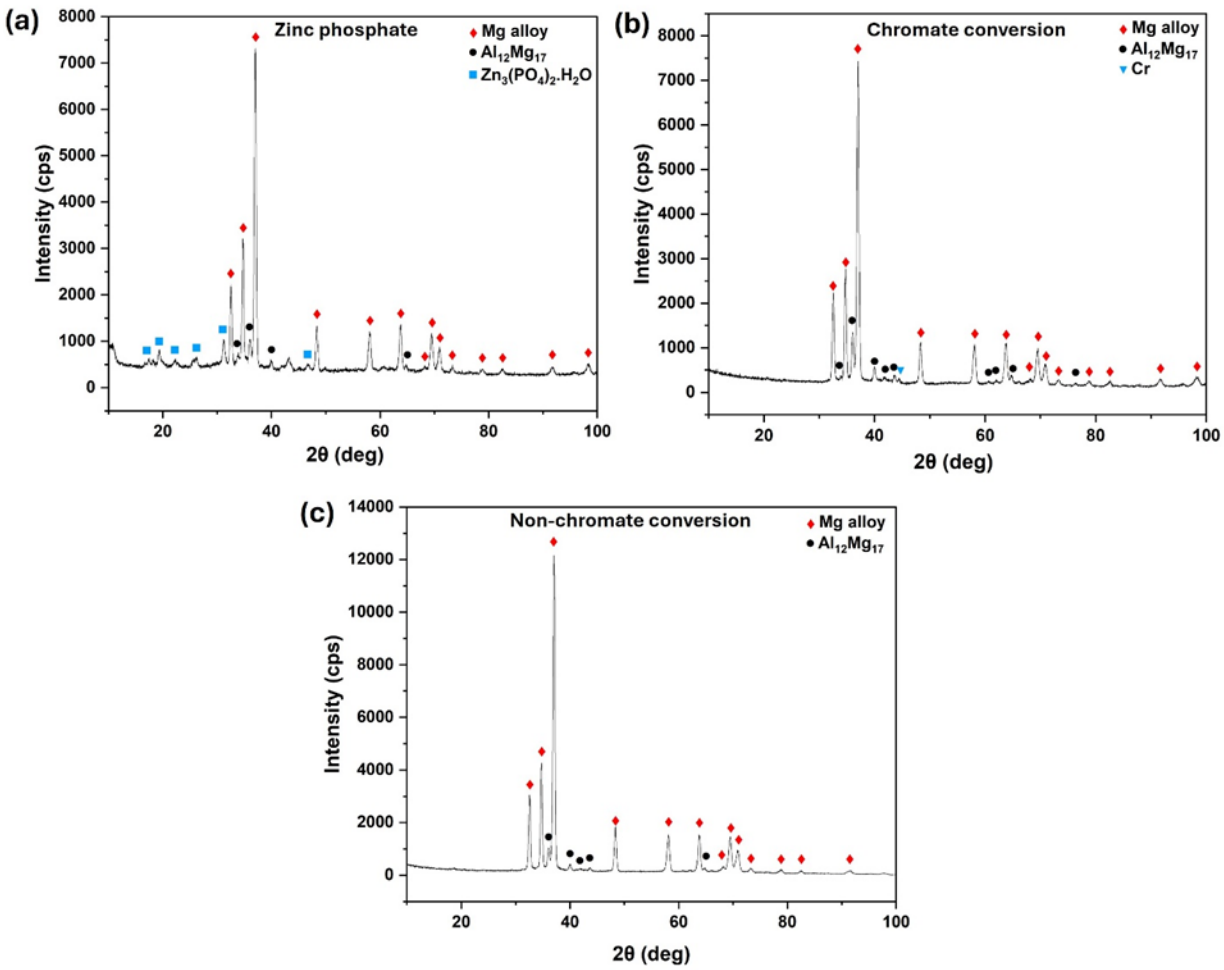

Figure 3: Grazing-incidence X-ray diffraction (GI-XRD) patterns of AZ91 Mg alloy surfaces subjected to different pre-treatments: (a) zinc phosphate, (b) chromate conversion, and (c) non-chromate conversion.

Figure 3 shows the GI-XRD patterns for all pre-treated surfaces. The dominant reflections in each of the pre-treatments correspond to the Mg matrix and the $Al_{12}Mg_{17}$ intermetallic, the latter being a well-known constituent phase in AZ91 alloys. The Mg reflections are indexed "Mg alloy" because their 2θ positions are slightly shifted relative to pure Mg; this shift is consistent with lattice parameter changes caused by alloying elements in solid solution (e.g., Al, Zn) that subtly alter interatomic spacing in the Mg matrix. The presence of $Al_{12}Mg_{17}$ is expected for this composition, as observed in figure 2, and appears with reproducible peak positions across investigated samples.

Pre-treatment specific signals are also evident. The zinc-phosphate treated surface shows additional peaks related to zinc phosphate hydrate ($Zn_3(PO_4)_2 \cdot H_2O$), confirming deposition of the coating layer (shown in figure 3(a)). In the chromate conversion coating (shown in figure 3(b)), a small signal at $2\theta \approx 44.5°$ was

observed and indexed to metallic Cr. Given its low intensity, this likely represents either small metallic inclusions, a very thin particulate layer, or incomplete oxidation/reaction within the conversion treatment. Conversely, the non-chromate conversion coating does not show this Cr feature (shown in figure 3(c)). Although a Ti signal was observed from SEM-EDS, it was not detected from XRD, which could be due to the Ti being dispersed at concentrations below the XRD detection limit.

3.2 Wear testing of pre-treatment coatings and Zn cold sprayed AZ91

Figure 4 represents the overall tribological response of bare AZ91D, pretreated AZ91D coupons, and the cold-sprayed Zn coatings. The variation in COF with sliding distance for all surface-modified AZ91D samples is shown in Figure 4(a). Nearly all pretreatment conditions produced a markedly shorter run-in period, typically under 5 m of sliding, after which the COF rapidly transitioned into a stable steady-state regime. In contrast, the cold-sprayed Zn coatings displayed significantly higher and irregular fluctuations in COF throughout the sliding test. [45,46] Interestingly, the cold-sprayed Zn coating exhibited comparatively smaller wear dimensions than the pretreated AZ91D substrates, as shown in Figure 4(b). The Zn coating produced a wear track with an average width of approximately 600 μm and a maximum wear depth of ~50 μm. In contrast, the various pretreatment conditions applied to AZ91D resulted in substantially larger wear track widths, generally exceeding 1000 μm. Although these AZ91D samples demonstrated relatively stable steady-state COF behavior, such stability does not necessarily correlate with reduced wear. Rather, the combination of higher COF values and broadened wear tracks suggests the dominance of severe abrasive wear mechanisms in the pretreated AZ91D substrates [47,48].

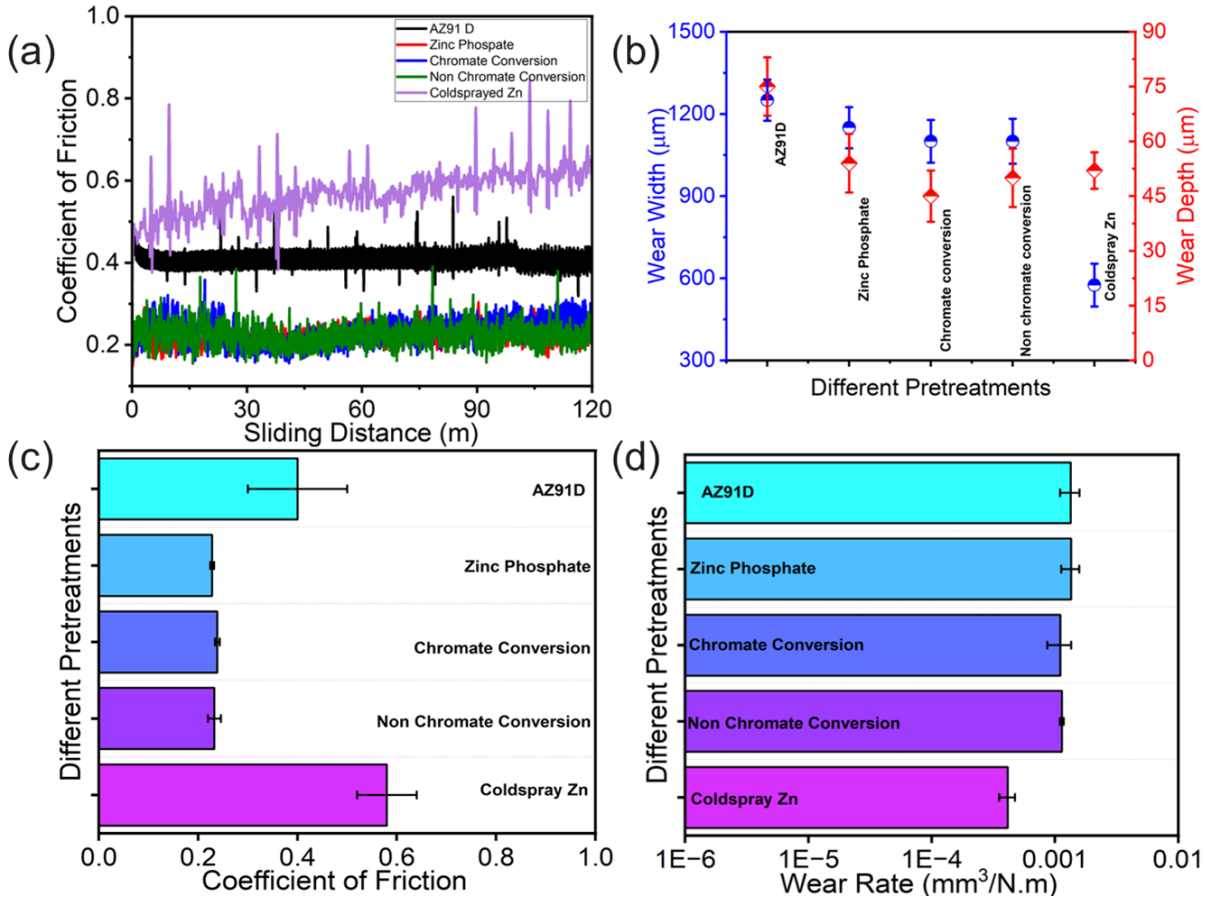

Figure 4: Wear testing of Zn coated AZ91 compared with uncoated AZ91 and pre-treated AZ91 samples, (a) Coefficient of Friction (CoF) versus Sliding Distance curves, (b) Wear Depth versus Wear Width plots, (c) Average CoF, and (d) Wear rate for all the different pretreatments on AZ91D Mg alloy

The steady-state COF values obtained for the pretreated AZ91D coupons ranged from approximately 0.23 ± 0.01 to 0.41 ± 0.08, as summarized in Figure 4(c). These values indicate that the various chemical pretreatments Zn phosphate, chromate conversion, and non-chromate conversion do not substantially elevate COF beyond that of the untreated AZ91D substrate. In contrast, the cold-sprayed Zn coating exhibited a significantly higher steady-state COF of 0.58 ± 0.06, consistent with the pronounced stick–slip and adhesion driven interactions discussed earlier. The corresponding sliding wear rates for each condition are presented in Figure 4(d). The Zn phosphate, chromate conversion, and non-chromate conversion pretreatments produced wear rates of $1.3 \pm 0.2 \times 10^{-3}$ mm³/N·m, $1.1 \pm 0.4 \times 10^{-3}$ mm³/N·m, and $1.1 \pm 0.2 \times 10^{-3}$ mm³/N·m, respectively, values comparable to that of the untreated AZ91D ($1.3 \pm 0.2 \times 10^{-3}$ mm³/N·m). These results suggest that while chemical pretreatments may influence the frictional response, they do not impart substantial improvements in wear resistance under the present loading and sliding

conditions. In contrast, the cold sprayed Zn coating demonstrated a markedly reduced wear rate ($4.1 \pm 0.6 \times 10^{-4}$ mm³/N·m), nearly an order of magnitude lower than any of the AZ91D-based treatments.

3.3 Corrosion Testing

3.3.1 Hydrogen collection measurements

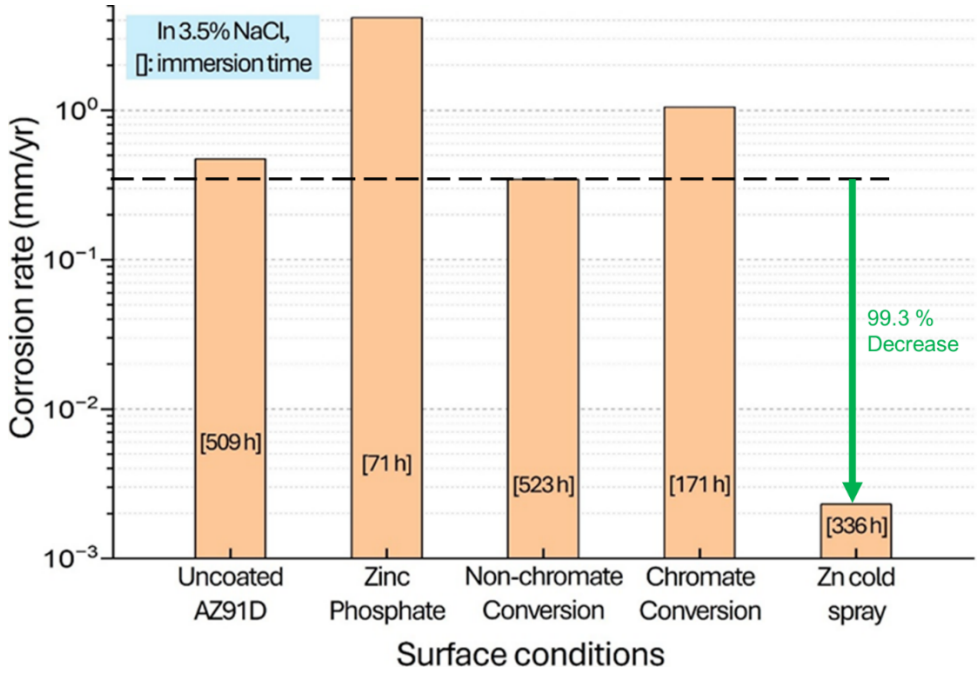

Figure 5: Corrosion rates (mm per year) converted from H_2 volume data for uncoated AZ91, zinc phosphate pre-treatment, non-chromate conversion, chromate conversion and Zn cold spray coating. The rates were calculated with one measurement per surface condition.

Figure 5. presents the corrosion rates converted from evolved H_2 volume data at specific immersion times in 3.5% NaCl. As noted in the rate data, two pretreatments, Zn phosphate and chromate conversion coatings, accelerated Mg corrosion of AZ91D. It is suspected that reduction of Zn and Cr ions, released in the NaCl solution, occurred by taking electrons from Mg (Mg anodic dissolution) because Zn and Cr are galvanically more noble than Mg. Non-chromate conversion coating showed only subtle reduction in Mg corrosion rate, which implies the pretreatment coating alone cannot protect Mg alloy substrate. Meanwhile, Zn sprayed surface showed a very low corrosion rate, which should be attributed to the protective barrier effect of compact Zn layer for the AZ91D substrate. Figure 5 shows that the Zn cold spray coating reduces the corrosion rate by atleast 99.3 %.

3.3.2 Multimodal corrosion testing- Simultaneous electrochemical testing and *in situ* imaging

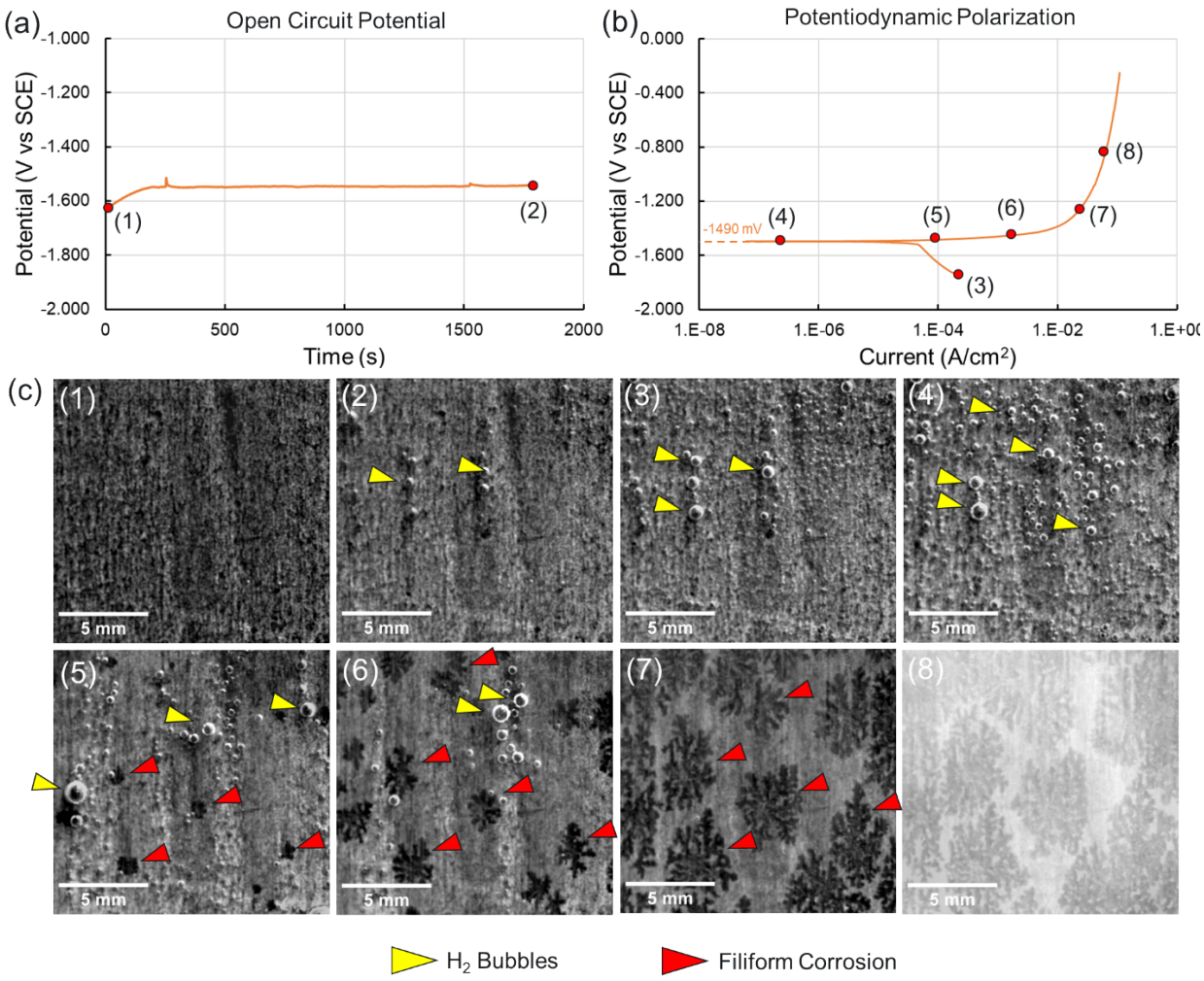

Figure 6: (a) OCP and (b) PD plots of zinc phosphate pre-treated AZ91 tested in 3.5 wt.% NaCl solution. (c) shows numbered images of the corroding sample at specific points on the OCP and PD curves as annotated by the numbers from 1 - 8.

Multimodal corrosion testing was performed on the three pre-treatment conditions, i.e. the zinc phosphate, chromate conversion and non-chromate coatings, compared with the corrosion results from the Zn cold spray coated AZ91. The analysis of the PD curves yielded the corrosion potential (E_{corr}), Corrosion current (A/cm^2), Anodic slope- βa (V/decade), Cathodic slope- βc (V/decade), Polarization Resistance-Rp ($\Omega.cm^2$) and Corrosion Rate (mpy) are summarized in Table I included in the supplementary section of the manuscript. Figure 6 shows the corrosion performance of zinc phosphate coated on AZ91 sample. Specifically, Figure 6(a) and 6(b) present the OCP and PD behaviors of the pre-treatment. The OCP was observed to stabilize at -1550 ± 5 mV (vs SCE) and the E_{corr} as measured using PD was measured to be -1490 mV (vs SCE). Figure 6(c) shows the surface images of the sample at specific locations during OCP

and PD curves in Figure 6(a) and 6(b). During the OCP, hydrogen bubble evolution (yellow pointers) in some locations was observed, indicating the initiation of localized corrosion without applied anodic potential (in the surface images c-1 and c-2). The hydrogen bubble evolution is a result of the corrosion reaction of Mg as described in the oxidation, reduction (combination of a hydrogen evolution reaction- HER and an oxygen reduction reaction- ORR) and net redox reaction stated below:

Anodic Reaction: $Mg \rightarrow Mg^{2+} + 2e^-$

Cathodic Reactions: HER: $2H_2O + 2e^- \rightarrow 2OH^- + H_2\uparrow$

ORR: $O_2 + 4e^- + 2H_2O \rightarrow 4\ OH^-$

Net Redox Reaction: $3Mg + O_2 + 4H_2O \rightarrow 3Mg(OH)_2 + H_2\uparrow$

During the cathodic polarization curve, the number of sites where hydrogen bubble initiates was observed to increase (in the surface image c-3). However, the rate of hydrogen bubble evolution was not observed to increase. Upon entering the anodic polarization regime after crossing the E_{corr}, the rate of hydrogen bubbles and number of sites, both increase substantially (in the surface image c-4). Following the E_{corr}, the current density increased notably leading to the first signs of local degradation of the surface. The surface image c-5 shows the presence of localized surface degradation appearing as pits at several locations on the surface as designated by the red pointers. These pits appear to expand and interconnect on the surface with increase in applied potential as shown in the surface images c-6 and c-7. While the number of pit sites increases marginally, the pits themselves exhibit a filiform growth mechanism emanating from the central pit location. This gives them the appearance of an ice crystal-shaped or dendrite-shaped filiform growth pattern that eventually coalesces at higher applied potentials. The surface image c-8 shows the example of very large (~ 5 mm in diameter) sized filiform growth patterns at potentials more noble than -800 mV (vs SCE). The image also appears hazy, and this is due to the presence of corrosion product from the sample in the solution at the high applied potential values.

Figure 7 shows the corrosion performance of chromate conversion pre-treatment coated on top of AZ91 plate sample. Figure 7(a) and (b) show the OCP and PD behaviors of the pre-treatment. The OCP was observed to equilibrate at -1550 ± 5 mV (vs SCE) and the E_{corr} was measured to be -1510 mV (vs SCE). Figure 7(c) shows inset images of the sample at specific locations on the OCP and PD curves of the sample. During the OCP, hydrogen bubble evolution (yellow pointers) in very small quantities was observed, indicating the initiation of localized corrosion at no applied potential (as shown in inset images c-1 and c-2).

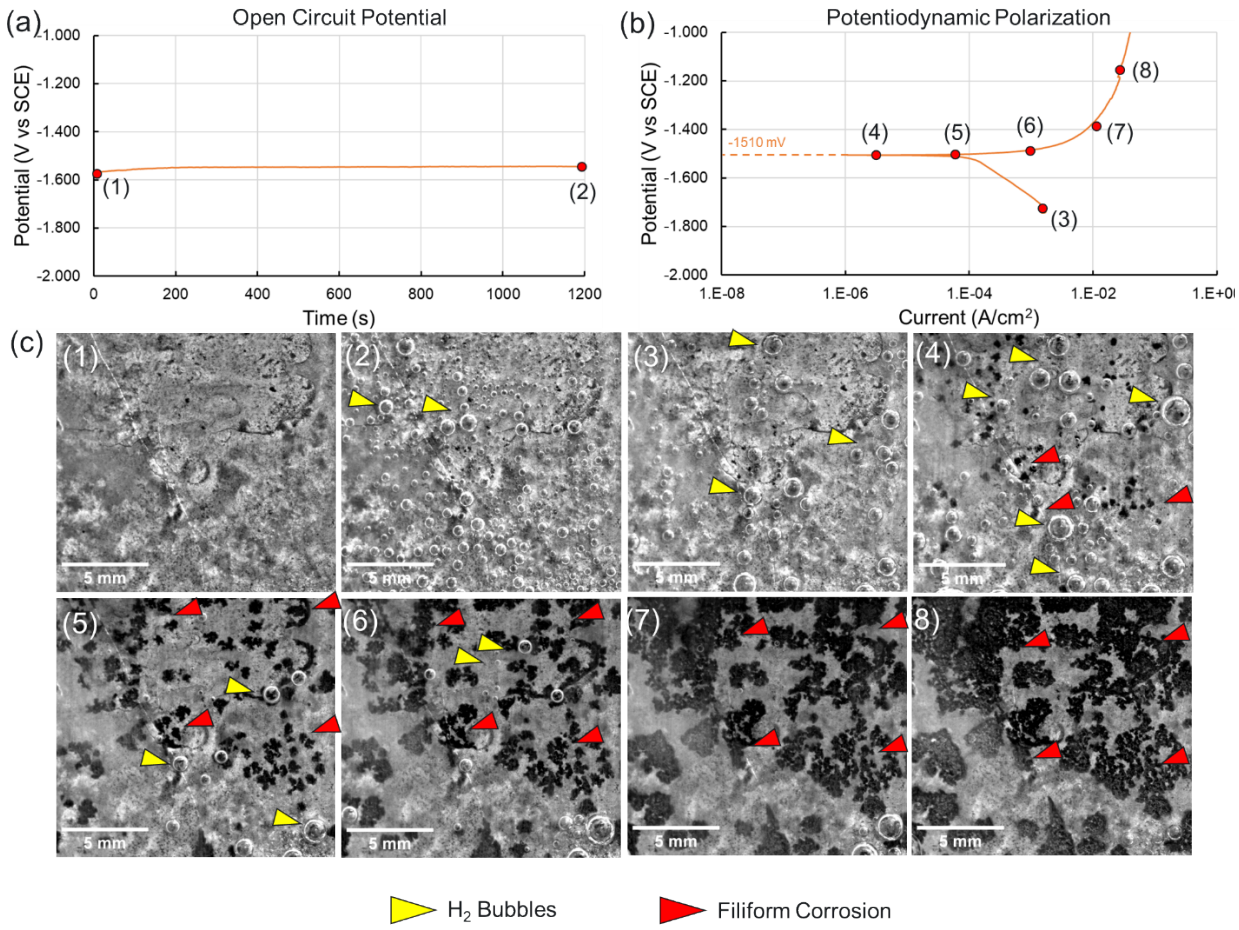

Figure 7: (a) OCP and (b) PD plots of chromate conversion pre-treated AZ91 tested in 3.5 wt.% NaCl solution. (c) shows numbered images of the corroding sample at specific points on the OCP and PD curves as annotated by the numbers from 1 - 8.

During the cathodic polarization curve, the number of sites where hydrogen bubble initiates was observed to increase (as shown in inset image c-3). However, the rate of hydrogen bubble evolution was not observed to increase. Upon entering the anodic polarization regime after crossing the E_{corr}, the rate of hydrogen bubble evolution and number of sites, both increase substantially (as shown in inset image c-4). Following the E_{corr}, the current density also increased notably leading to the first signs of local degradation of the surface in the form of several localized pits as shown using red pointers. These pits appear to grow with increase in applied potential as shown by inset images c-5, c-6 and c-7. The pits also start coalescing readily and do not show a filiform corrosion pattern as seen in the zinc phosphate sample. Instead, the corrosion mechanism involves exfoliation of chunks of the coating on the surface. At these applied potentials, the rate of hydrogen evolution is very rapid due to the exposed AZ91 surface. As seen in inset image c-8, the surface

degradation worsens with increase in applied potential until more than 50% of the area of the sample is corroded upon reaching an applied potential of -1200 mV (vs SCE).

Figure 8 shows the corrosion performance of non-chromate conversion pre-treatment coated on top of AZ91 plate sample. Figure 8(a) and (b) show the OCP and PD behaviors of the non-chromate pre-treatment. The OCP was observed to equilibrate at -1590 ± 10 mV (vs SCE) and the E_{corr} was measured to be -1530 mV (vs SCE). Figure 8(c) shows inset images of the sample at specific locations on the OCP and PD curves of the sample. During the OCP, hydrogen bubble evolution (yellow pointers) in very small quantities was observed, indicating the initiation of localized corrosion at no applied potential (as shown in inset images c-1 and c-2). During the cathodic polarization curve, the number of sites where hydrogen bubble initiates was observed to increase (as shown in inset image c-3). However, the rate of hydrogen bubble evolution was not observed to increase.

Upon entering the anodic polarization regime after crossing the E_{corr}, the rate of hydrogen bubble evolution and number of sites, both increase substantially (as shown in inset image c-5). Following the E_{corr}, the current density also increased notably leading to the first signs of local degradation of the surface. Inset image c-5 shows the presence of localized surface degradation appearing as pits at several locations on the surface as shown by the red pointers. These pits appear to grow with increase in applied potential as shown by inset images c-6 and c-7. The pits themselves exhibit a filiform growth mechanism emanating from the central pit location with no notable increase in number of such pit sites indicating that the current density is localized around the filiform corrosion growth fronts. Similar to the zinc phosphate pre-treatment, the filiform corrosion pattern appear ice-crystal-shaped or show a dendrite-shaped filiform growth pattern that eventually coalesce at higher applied potentials. Certain pit sites also exhibit long filiform corrosion extensions (seen in inset images c-6 and c-7) that upon careful observation travel along pre-existing scratches on the surface of the pre-treatment. However, it is important to note that the pre-existing scratches had not exposed the AZ91 substrate underneath, until the filiform corrosion front passed through it. Finally, inset image c-8 shows these filiform growth patterns coalescing at potentials more noble than -800 mV (vs SCE).

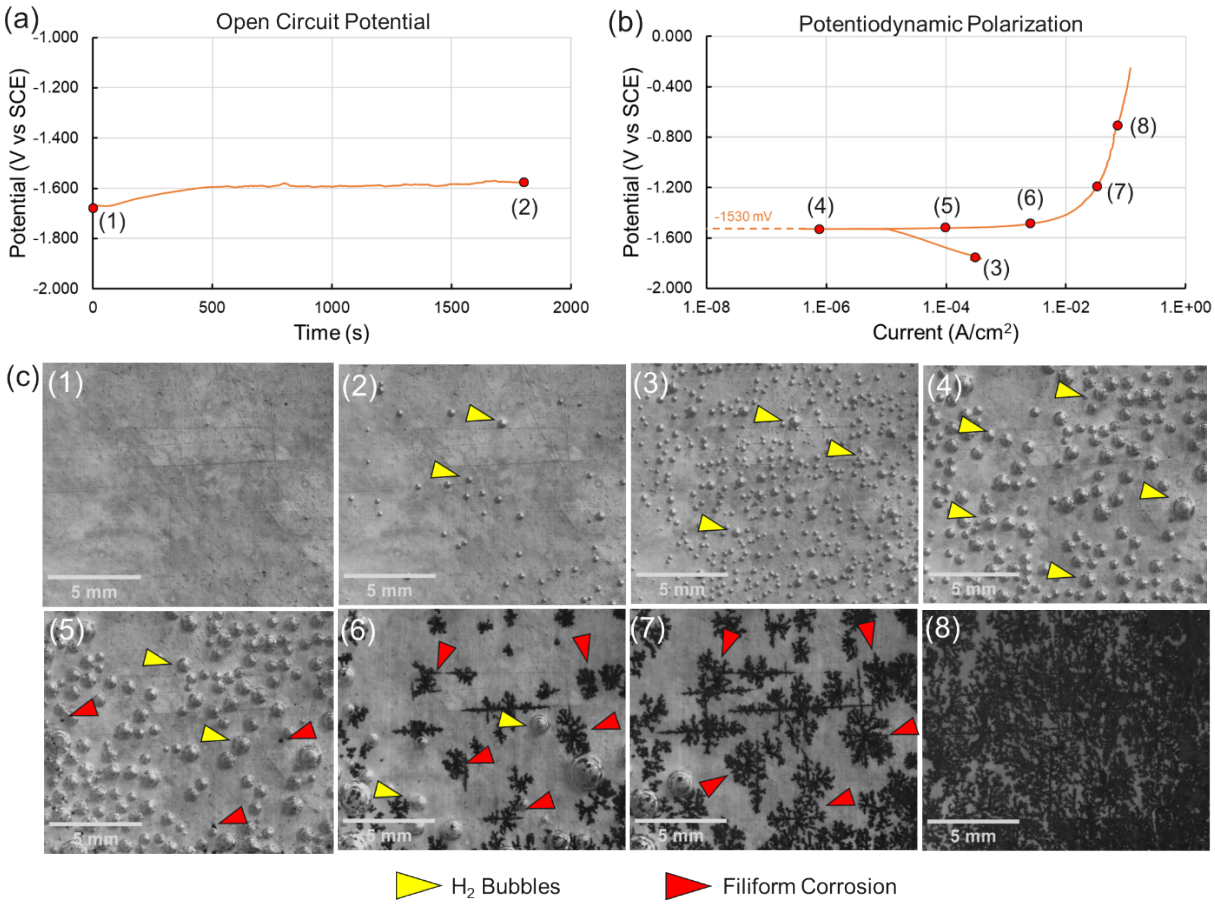

Figure 8: (a) OCP and (b) PD plots of non-chromate conversion pre-treated AZ91 tested in 3.5 wt.% NaCl solution. (c) shows numbered images of the corroding sample at specific points on the OCP and PD curves as annotated by the numbers from 1 - 8.

Finally, Figure 9 shows the corrosion performance of as-deposited Zn cold spray coated on top of AZ91 plate sample. Figure 9(a) and (b) show the OCP and PD behaviors of the pre-treatment. The OCP was observed to equilibrate at -1070 ± 5 mV (vs SCE) and the E_{corr} was measured to be -1060 mV (vs SCE). Figure 9(c) shows inset images of the sample at specific locations on the OCP and PD curves of the sample. During the OCP, the Zn cold spray coating, unlike the pre-treatments shown in figures 6, 7 and 8, does not show the release of any hydrogen bubbles. The sample remains unchanged over the course of the OCP and the cathodic polarization curves.

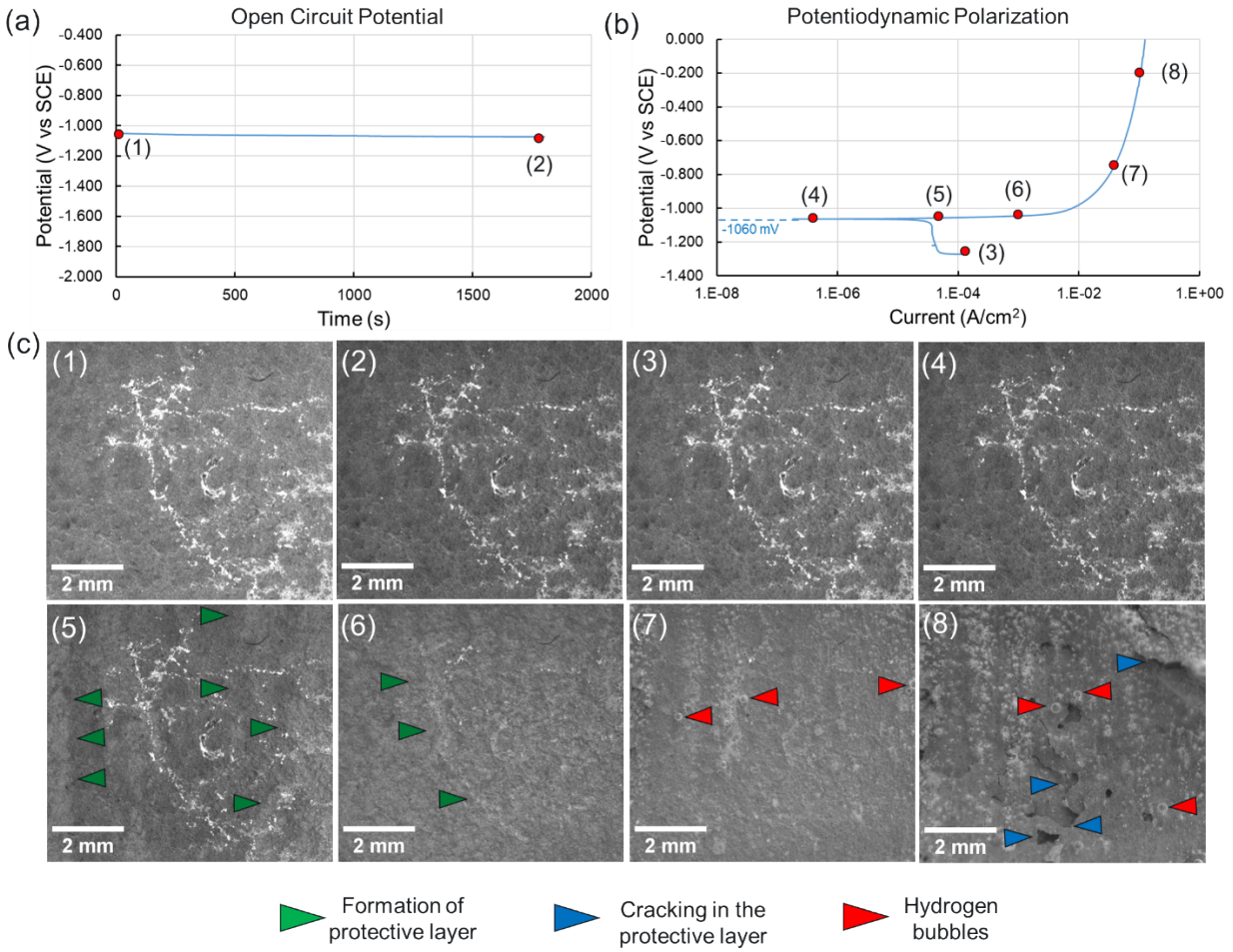

Figure 9: (a) OCP and (b) PD plots of Zn cold spray coated AZ91 tested in 3.5 wt.% NaCl solution. (c) shows numbered images of the corroding sample at specific points on the OCP and PD curves as annotated by the numbers from 1 - 8. The protective layer/patina forms on the surface of the Zn cold spray coating and covers the entirety of the surface as seen in figure (c-6).

Upon entering the anodic polarization regime after crossing the E_{corr}, the Zn coating begins to form a surface protective layer on the surface that can be seen to form in inset image c-5 (as shown using a green arrows). This surface layer covers the entirety of the surface as shown in inset image c-6 that remains intact until -800 mV (vs SCE). Following this, the surface exhibits signs of the disintegration of the protective layer by forming cracks (blue arrows in inset image c-7) at potential values below -800 mV (vs SCE). At an applied anodic potential of -200 mV (vs SCE), the protective layer cracks and falls off of the surface leaving behind the rest of the Zn cold spray coating underneath (as shown in inset image c-8). Notably, the AZ91 surface does not get exposed after the protective patina / layer degrades as evidenced by the lack of rapid hydrogen bubble release at the very noble applied potentials. However, small quantities of hydrogen bubbles form on

the surface, particularly from cracks in the protective layer at the high anodic potentials (Figure 9 (c-7 and 8)).

4. Discussion

The results presented in this manuscript present an important step in comparing and implementing Zn cold sprayed coatings as a pre-treatment coating for automotive HPDC Mg alloys. The microstructure of the pre-treatments as shown using SEM and EDS results (figure 2) and XRD results (Figure 3) offer a glimpse into the chemical compositional complexity of the coatings and their associated processing methods. The pre-treatment coatings presented in this study utilize chemical processes that present significant challenges in terms of their safe handling and disposal. For example, the zinc phosphate coating process, while effective in covering the surface of the Mg alloys, results in the generation of significant volumes of sludge-waste products that present a safe disposal challenge to the automotive industry [28]. Similarly, the automotive industry also implemented chromate conversion coatings that traditionally utilized hexavalent chromium, a highly toxic and carcinogenic species, and have since moved on to a safer alternative- trivalent chromate systems and non-chromate alternatives. The development and implementation of pre-treatments that pose no health or environmental concerns is therefore of high importance to the automotive industry and Zn cold spray coating using metallic Zn powders offers a potential solution by eliminating aqueous chemical waste streams and the use of regulated Cr-bearing species.

Wear testing results indicate that the wear rate of the Zn cold spray coating is lower than the uncoated AZ91 and the pre-treatment coatings. The COF of the various pretreated AZ91D substrates was nearly 50% lower than that of the bare AZ91D alloy. This reduction can be attributed to the influence of surface pretreatments in relatively reducing the plastic deformation during sliding. The modified surface layers provide enhanced load-bearing capacity, thereby limiting severe plowing of the soft Mg matrix. In addition, the wear debris generated from the pretreated surfaces tends to undergo compaction and smearing within the wear track, forming a mechanically mixed tribo-layer. This smeared debris layer acts as a protective third body, reducing direct asperity–asperity contact and suppressing abrasive interactions resulting in decrease in COF during sliding. Such behavior is characteristic of a pronounced stick–slip phenomenon, wherein irregular adhesion and sudden release events occur at the contact interface [45,46]. The tendency for strained Zn to undergo localized plastic deformation and fracture under the applied contact stresses further worsens this effect. As the coating material is progressively detached during sliding, wear debris can adhere to the counterface. This adhered material increases the real contact area, thereby intensifying adhesion driven by frictional forces. The combined influence of stick–slip condition, intermittent material transfer, and the enlarged interfacial contact area contributes to the larger fluctuations in COF observed for the Zn coating.

The comparatively lower wear rates observed for the cold-sprayed Zn coatings, relative to the bare and pretreated AZ91D substrates, cannot be explained solely on the basis of hardness [49,50] and instead reflect the combined influence of multiple mechanical and tribological parameters, particularly fracture toughness [51] and dominant wear mechanisms. Although the hardness of the cold-sprayed Zn coating (~43 ± 2 HV) is significantly lower than that of the AZ91D and pretreated AZ91D substrates (~61 ± 9 HV), the Zn coating exhibits superior wear resistance. This behavior deviates from the classical Archard's wear law, which predicts an inverse relationship between hardness and wear rate. Such deviation indicates that hardness alone is not the governing parameter in this system. The enhanced wear performance of the cold-sprayed Zn coating can be attributed to its relatively higher fracture toughness and the associated transition in wear mechanisms, which suppresses severe abrasive and adhesive wear. Mg alloys exhibit significantly lower fracture toughness (~6-10 $MPa \cdot m^{1/2}$) [52] compared to Zn-based systems [53,54], which renders them more susceptible to crack initiation and rapid crack propagation under sliding contact leading to the generation of a larger volume of wear debris. The detached debris further acts as third-body abrasives, intensifying material removal and resulting in an increased wear rate and greater overall material loss during sliding. A similar behavior was observed, wherein the $Mg_{17}Al_{12}$ intermetallic particles became dislodged during sliding and adhered to the counterface, subsequently reacting to form $MgAl_2O_4$, which acted as a third-body abrasive layer, promoting enhanced material removal during continued sliding [55]. In case of cold sprayed Zn coating, the lower wear rate is primarily attributed to the peening effect induced by individual Zn particles during the cold spray deposition process, which results in severe plastic deformation and pronounced work hardening of the coating. This reduces the real area of contact during sliding, thereby suppressing both abrasive plowing and adhesive junction growth and leading to a substantial reduction in material loss. Furthermore, although the effective fracture toughness of the cold-sprayed Zn coatings (~25–40 $MPa \cdot m^{1/2}$) [53,54] may be slightly diminished due to the presence of inter-splat boundaries and residual porosity, it remains sufficiently high to inhibit crack propagation and delamination. This resistance to brittle fracture favors mild adhesive wear as the dominant mechanism, further contributing to the reduced wear rate.

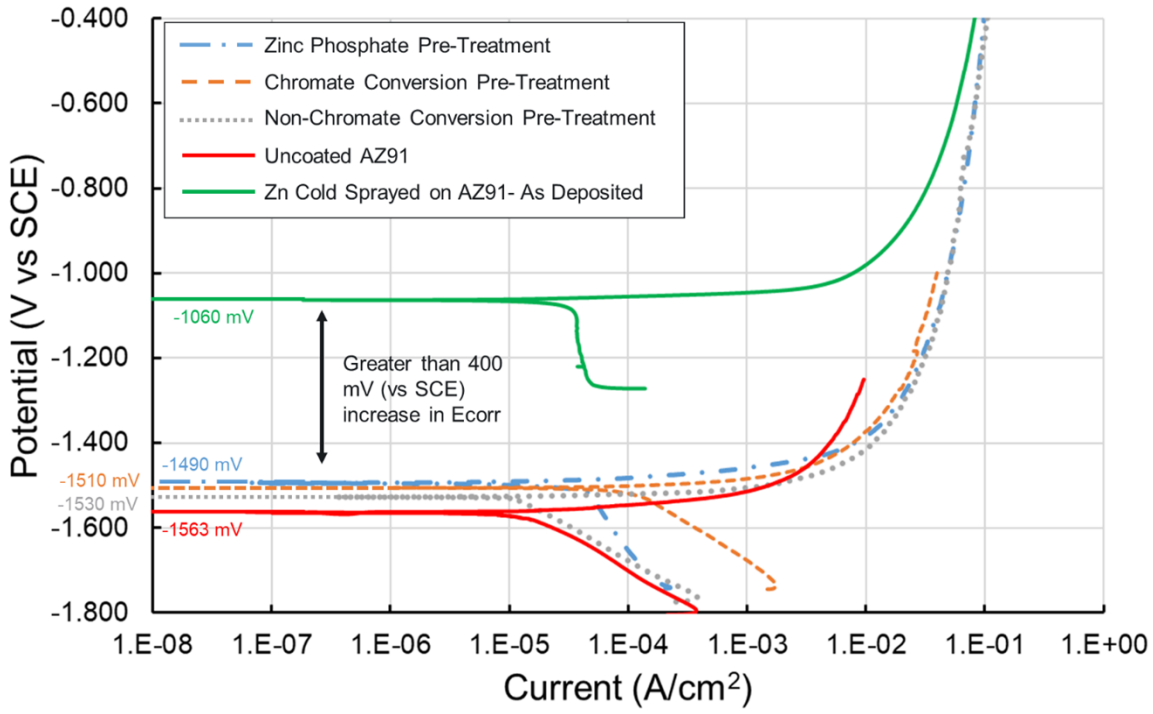

Figure 10: Overlay of the PD measurements from uncoated AZ91, pre-treated (zinc phosphate, chromate conversion and non-chromate conversion) AZ91 and Zn cold spray coated AZ91 samples.

Electrochemical testing and hydrogen collection measurements both indicate that the Zn cold spray coating's E_{corr} is more noble, and the rate of corrosion (mpy) is lower compared to the uncoated AZ91 and the pre-treatment coatings. Figure 10 summarizes the PD behaviors of uncoated AZ91, pre-treated AZ91 and Zn coated AZ91. The uncoated AZ91 exhibits an E_{corr} value of -1563 mV (vs SCE), which is consistent with observations in the literature [42]. The pre-treatment coatings increase the E_{corr} by an average of ~50 mV (vs SCE), making the AZ91 alloy behave nobly. However, this magnitude of increase in E_{corr} is significantly smaller than the increase in E_{corr} brought about by the Zn cold spray coating. The Zn coating has an E_{corr} of -1060 mV (vs SCE) as shown in this study. This value is atleast 400 mV greater (more noble) than that exhibited by the pre-treatment coatings and ~500 mV greater than that exhibited by the uncoated AZ91. This more noble E_{corr} indicates that the Zn cold spray coating has a much lower propensity to participate in the corrosion process, as compared to the pre-treatments and the uncoated AZ91. The Zn cold spray coating forms a protective coating during the corrosion process that protects the surface from further exposure to the corrosive fluid. The formation of a protective coating is a result of the oxidation and reduction reactions of the Zn corrosion process as shown below:

Anodic Reaction: $Zn \rightarrow Zn^{2+} + 2\ e^-$

Cathodic Reactions: Hydrogen Evolution Reaction (HER): $2\ H_2O + 2\ e^- \rightarrow 2OH^- + H_2\uparrow$

Oxygen Reduction Reaction (ORR): $O_2 + 4\ e^- + 2\ H_2O \rightarrow 4\ OH^-$

Net Redox Reaction: $Zn + 2\ H_2O \rightarrow Zn\ (OH)_2 + H_2\uparrow$

$Zn(OH)_2 \rightarrow ZnO + H_2O$

Additionally, in the presence of Cl^- ions in the solution, the following reaction can take place resulting in the formation of zinc hydroxy chloride [56].

$$5\ Zn^{2+} + 8\ OH^- + 2\ Cl^- + H_2O \rightarrow Zn_5(OH)_8Cl_2 \cdot H_2O$$

Thus, the protective coating forming on the surface is a possible combination of ZnO, $Zn(OH)_2$ and $Zn_5(OH)_8Cl_2 \cdot H_2O$. The determination of the precise chemical composition of the coating is an ongoing effort and is beyond the scope of this study. The absence of H_2 bubble release during OCP, cathodic polarization and early anodic polarization of Zn in aerated salt solution (figure 9) is consistent with a preference for the ORR as the dominant cathodic reaction taking place on the surface. The preference for the ORR over the HER is due to the neutral pH of the salt solution used, leading to lesser proton activity (unlike in acidic solutions). Furthermore, there is an absence of localized pit formation on the Zn surface (in contrast to that seen on the AZ91 substrate [42]), and thus no development of occluded regions characterized by depleted oxygen and locally acidified conditions. In AZ91, such pit environments formed around microgalvanic couples in the microstructure (at $Mg_{17}Al_{12}$/ Mg-matrix interface or Fe-rich intermetallic particle/Mg-matrix interface) promote a shift in the dominant cathodic process from oxygen reduction to the HER, thereby facilitating measurable H_2 bubble nucleation, growth, and detachment [42]. Due to this, we observe no H_2 bubbles during the formation of the protective layer/patina on the Zn cold spray coating. However, once the layer begins to crack at high applied anodic potentials, H_2 bubble nucleation is possible (as seen in Figure 9 (c-7 and 8)) within the cracks due to localized oxygen depletion and a shift from ORR to HER as the dominant cathodic reaction [56]. Only at potentials nobler than -400 mV (vs SCE), the protective layer appears to break and exfoliate off of the surface, leaving behind a still intact coating of cold sprayed Zn.

On the other hand, the pre-treatments or uncoated AZ91 undergo significant pitting and filiform corrosion attack under anodic polarization exposing the AZ91 substrate underneath. The reason for the origin of pits in the pre-treatments was likely initiated from sites containing pre-existing intermetallic particles in the microstructure (creating a microgalvanic couple between the particle and pre-treatment coating) or from areas where the coating was cracked, discontinuous and / or its thickness was non-uniform (as shown in figure 2) . An example of this can be seen in the non-chromate coating condition where the filiform

corrosion is traced along pre-existing scratches on the surface of the coating (as seen in figure 8). During filiform corrosion, the corrosive electrolyte penetrates in between the coating-substrate interface, corrodes the Mg substrate and forms corrosion products and H_2 bubbles (due to favorable HER as compared to ORR inside the crevice) that push/blister the coating and potentially fracture it [57]. The ease of coating fracture depends on the mechanical properties of the coating and how many layers comprise it, with some thicker coatings showing the presence of corrosion tunnels or vein-like structures where the corrosion has progressed sub-surface but not fractured the coating. The filiform corrosion front is reported to be anodically active while the regions immediately behind the front i.e., the filiform corrosion trail, is measured to be cathodically active. An active supply of chloride ions with the corrosive fluid assists in maintaining the corrosion current within the filament enabling the continuous propagation of the filiform corrosion front. The propagation of the filiform corrosion front stops when the supply of chloride ions and corrosive fluid is stopped [57–60]. In the pre-treatment coatings, the fracture of the pre-treatment coatings due to blistering at the filiform corrosion front, and continuous ingress of new corrosive fluid enables the front to propagate freely without termination. The precise reason that filiform corrosion develops a star-like or snowflake pattern can be attributed to individual branches propagating along favorable crystallographic planes, dictated by the crystal orientations of grains surrounding the corroding pit [61,62].

The adhesion strength of cold spray coatings plays a key role in determining their long term durability [32,33]. In a previously published study by the same authors, the adhesion strength of coatings deposited using various cold spray carrier gas parameters was measured using ASTM D4541 [33]. Results showed that the optimized cold spray parameters (same as the parameters used in this study) exhibited adhesion strength values exceeding 30 MPa and coupon failure mechanism. During electrochemical corrosion of cold sprayed Zn as demonstrated in this study and long term immersion in salt water environment (as demonstrated in [33]), we do not observe any coating delamination, sub-surface intergranular corrosion, exfoliation corrosion or the formation of corrosion tunnels- a corrosion phenomenon that has been reported in Zn cold spray coatings [63]. Instead, we observed the formation of a protective film on the surface that prevents sub-surface corrosion. Furthermore, the corrosion resistance of the cold sprayed Zn coating is maintained irrespective of whether the coating is 2 passes thick (~300-400 μm as in this study) or 10 passes thick (~ 1500 - 2000 μm), as shown in Figures S1 (1 pass at 45 degrees followed by 2 passes at 90 degrees spray angle- 1200 grit finish), Figure S2 (1 pass at 45 degrees followed by 10 passes at 90 degrees spray angle- 1 μm diamond finish) and Figure S3 (comparison of Zn coatings of different thicknesses and surface finishes) in the supplementary section of the manuscript. In other words, the mechanism of corrosion protection, i.e., the formation of a fresh protective layer on the Zn surface, occurs irrespective of coating thickness as well as initial surface roughness. A thin coating (fewer cold spray passes) is preferable as compared to thick coatings from the standpoints of weight savings, speed of coating application and

quantity of coating material used. The fact that the mechanism of corrosion remains the same irrespective of coating thickness and finish shows that the coating offers a reliable and predictable long term corrosion behavior.

Cold spray applicators can be mounted onto robotic systems, which can be programmed to selectively coat specific locations such as fastener regions and multimaterial interfaces on large, mega- and gigacastings, repeatedly. This highlights a viable path for scaling cold spray coating technology into automotive production lines. Additional work is needed to assess the viability of the cold sprayed Zn with downstream electrocoat (E-coat) and topcoat/powder-coat deposition which is critical for both surface protection as well as aesthetics. The combination of improved performance due to cold spray and a viable path for scaling brings us closer to further implementing Mg alloys in automobiles.

5. Conclusions

In this study, the newly developed and optimized Zn cold spray coating was coated onto AZ91 plate samples, and its microstructure and performance were evaluated and compared with uncoated AZ91 and with three widely used pre-treatments namely the zinc phosphate pre-treatment, the chromate conversion pre-treatment and the non-chromate conversion pre-treatment coatings. Our findings show the following:

- The pre-treatment coatings are measured to be between 0.5 – 5 μm in thickness and contain several elements within them that are a result of their processing history. They are also observed to be highly discontinuous and, as a result, may not perform as intended.
- The Zn cold spray coating shows a wear rate that is greater than 50% lower than the wear rates measured on the pre-treatment coatings.
- The hydrogen collection results indicate that the corrosion rate measured in the Zn coating is atleast 99.3 % lower as compared to those measured in the pre-treatment samples.
- Multimodal corrosion that combined electrochemical testing and *in situ* sample imaging was used to corrode the samples as well as visualize the ongoing corrosion damage in real time. The pre-treatment coatings, like uncoated AZ91, demonstrated a filiform or exfoliation corrosion mechanism of corrosion. However, the Zn cold spray coating formed a protective layer (comprising ZnO, $Zn(OH)_2$ and $Zn_5(OH)_8Cl_2 \cdot H_2O$) that eliminated the possibility of pitting, filiform or exfoliation corrosion on the surface and only fractured at very noble applied potentials, leaving behind more of the Zn coating underneath. The E_{corr} of the Zn coating was measured to be greater than 400 mV (vs SCE) more noble than that of the pre-treatments and uncoated AZ91, indicating a lower propensity to participate in corrosion processes.

Cold spray coatings are also scalable to the automotive production line due to the ease of mounting the applicator on to robotic arms. They also offer significant control over coating thickness, coating properties and performance. This, in combination with the overall improvement in wear and corrosion performance as compared to the pre-treatments studied and the uncoated AZ91 indicate that the Zn cold spray coatings are a viable pre-treatment option for Mg alloy surfaces, especially at vulnerable locations such as in the vicinity of multimaterial joints or along parting lines.

6. Supplementary Material

Please refer to the attached Supplementary Materials file.

7. Author Contributions

- Sridhar Niverty: Conceptualization, cold spray experiments, characterization, manuscript drafting and editing
- Mayur Pole: Characterization, manuscript drafting and editing
- Jijo Christudasjustus: Characterization, manuscript drafting and editing
- Jiheon Jun: Characterization, manuscript drafting and editing
- James V Haag: Characterization, manuscript drafting and editing
- Tanvi A Ajantiwalay: Characterization, manuscript drafting and editing
- Rajib Kalsar: Conceptualization, cold spray experiments, manuscript drafting and editing
- Vineet V Joshi: Conceptualization, manuscript drafting and editing, project management and funding acquisition

8. Data Availability

Data can be made available at reasonable request to the corresponding authors.

9. Acknowledgements

The authors acknowledge the support of the U.S. Department of Energy's Vehicle Technologies Office. The authors express their gratitude to ACT Test Panels LLC., for providing the pre-treatment coating services. The authors are grateful to Justin Olson and Mark Rhodes for assisting with cold-spray experiments, Alan Schemer Kohrn for support with characterization and Jorge Ortiz with sample preparation. Pacific Northwest National Laboratory is operated by Battelle for the U.S. Department of Energy under contract DE-AC06-76LO1830. We would also like to thank the reviewers of JOM for their valuable feedback and recommendations on the manuscript.

10. Declaration of Interest

On behalf of all authors, the corresponding author states that there is no conflict of interest.

11. References

1. A. A. Luo, Jom **54**, 42 (2002).

2. M. P. Brady, D. N. Leonard, H. M. M. Iii, J. K. Thomson, K. A. Unocic, H. H. Elsentriecy, G. Song, K. Kitchen, and B. Davis, Surf. Coat. Technol. **294**, 164 (2016).

3. Y. C. Lim, J. Chen, D. N. Leonard, M. P. Brady, and C. D. Warren, J. Manuf. Sci. Eng. **143**, (2021).

4. B. Liu, J. Yang, X. Zhang, Q. Yang, J. Zhang, and X. Li, J. Magnes. Alloy. **11**, 15 (2023).

5. M. P. Brady, W. J. Joost, and C. D. Warren, Corrosion **73**, 452 (2017).

6. J. P. Weiler, J. Magnes. Alloy. **7**, 297 (2019).

7. E. Siemionek, K. Majerski, P. Surdacki, and E. Novakova-Marcincinova, Adv. Sci. Technol. Res. J. **17**, 245 (2023).

8. O. Lunder, J. E. Lein, T. K. Aune, and K. Nisancioglu, Corrosion **45**, 741 (1989).

9. O. Lunder, J. E. Lein, S. M. Hesjevik, T. K. Aune, and K. Nişancioğlu, Mater. Corros. **45**, 331 (1994).

10. D. Hawke and K. Gaw, in *SAE Mobilus* (1992).

11. J. Jekl, J. Auld, C. Sweet, A. D. Klarner, J. Brevick, and A. A. Luo, 1 (2015).

12. S. Annamalai, S. Periyakgoundar, K. Paramasivam, and A. B. Selvaraj, Adv. Mater. Sci. Eng. **2020**, (2020).

13. R. W. Murray and J. E. Hilis, in *Int. Congr. Expo.* (1990).

14. P. Dauphin-ducharme and J. Mauzeroll, ACS Anal. Chem. **87**, 7499 (2015).

15. S. Thomas, N. V Medhekar, G. S. Frankel, and N. Birbilis, Curr. Opin. Solid State Mater. Sci. **19**, 85 (2015).

16. J. R. Kish, Y. Hu, J. Li, W. Zheng, and J. R. McDermid, Corrosion **68**, 468 (2012).

17. M. P. Brady, G. Rother, L. . Anovitz, K. C. Littrell, K. A. Unocic, H. H. Elsentriecy, G. L. Song, J. K. Thomson, N. C. Gallego, and B. Davis, J. Electrochem. Soc. **162**, C140 (2015).

18. J. Jun, Y. C. Lim, Y. Li, C. D. Warren, and Z. Feng, Mater. **14**, (2021).

19. Y. C. Lim, J. Jun, D. N. Leonard, Y. Li, J. Chen, and M. P. Brady, J. Magnes. Alloy. **10**, 400 (2022).

20. J. Jun, V. V. Joshi, A. Crawford, V. Viswanathan, D. N. Leonard, J. Chen, P. Updadhyay, Y. C. Lim, and Z. Feng, J. Magnes. Alloy. (2023).

21. A. Sharma, V. Beura, D. Zhang, J. Darsell, S. Niverty, V. Prabhakaran, N. Overman, D. R. Herling, V. Joshi, and K. Solanki, J. Magnes. Alloy. **12**, 3553 (2024).

22. H. F. Guo and M. Z. An, Appl. Surf. Sci. **246**, 229 (2005).

23. M. Laleh, F. Kargar, and A. Sabour Rouhaghdam, J. Coatings Technol. Res. **8**, 765 (2011).

24. M. P. Brady, D. N. Leonard, E. A. Mcnally, J. R. Kish, H. M. Meyer, E. Cakmak, and B. Davis, J. Electrochem. Soc. **166**, (2019).

25. J. Jun, Y. F. Su, J. E. Wade, D. Pappas, A. Sy, R. Robinson, and Y. C. Lim, J. Coatings Technol. Res. (2024).

26. G. G. Jang, J. Jun, J. K. Keum, Y. F. Su, M. Pole, S. Niverty, and V. V. Joshi, RSC Adv. **14**, 17696 (2024).

27. Y. Su, G. G. U. G. Jang, and J. E. W. Iv, JOM **77**, 3735 (2025).

28. M. Doerre, L. Hibbitts, G. Patrick, and N. Akafuah, Coatings **8**, (2018).

29. B. Liu, J. Yang, X. Zhang, Q. Yang, J. Zhang, and X. Li, J. Magnes. Alloy. **11**, 15 (2023).

30. M. P. Brady, W. J. Joost, and C. D. Warren, Corrosion **73**, 452 (2017).

31. K. Lazarz, J. Cahill, T. J. Ciccone, K. Redlin, and S. Simko, SAE Tech. Pap. 1 (2021).

32. T. Ajantiwalay, L. Li, J. V Haag IV, S. Niverty, R. Kalsar, A. Devaraj, A. Soulami, and V. V Joshi, J. Magnes. Alloy. **13**, 4877 (2025).

33. S. Niverty, R. Kalsar, L. Li, N. R. Overman, J. Jun, J. V Haag, T. A. Ajantiwalay, M. Pole, and V. V Joshi, J. Magnes. Alloy. (2025).

34. S. Niverty, R. Kalsar, A. J. Naccarelli, T. J. Eden, X. Ma, N. Overman, G. Grant, D. Herling, and V. V. Joshi, Mater. Des. **238**, (2023).

35. R. Kalsar, S. Niverty, M. Pole, J. V. Haag, T. Ajantiwalay, and V. V. Joshi, Mater. Charact. **232**, 115950 (2026).

36. M. Hassani-Gangaraj, D. Veysset, V. K. Champagne, K. A. Nelson, and C. A. Schuh, Acta Mater.

158, 430 (2018).

37. M. Hassani, V. K. Champagne, and D. Helfritch, Adv. Cold Spray a Coat. Depos. Addit. Manuf. Process **0**, 149 (2023).

38. H. Assadi, H. Kreye, F. Gärtner, and T. Klassen, Acta Mater. **116**, 382 (2016).

39. F. G. T. S. H. K. H Assadi, Acta Mater **51**, 4379 (2003).

40. M. Daroonparvar, H. R. Bakhsheshi-Rad, A. Saberi, M. Razzaghi, A. K. Kasar, S. Ramakrishna, P. L. Menezes, M. Misra, A. F. Ismail, S. Sharif, and F. Berto, J. Magnes. Alloy. **10**, 2025 (2022).

41. ASTM E 384-09, ASTM Int. West Conshohocken, PA, United States **384**, 399 (1999).

42. S. Niverty, R. Kalsar, R. J. Seffens, A. D. Guzman, T. J. Roosendaal, L. Strange, and V. V Joshi, Sci. Reports | **13**, 16695 (2023).

43. M. Stern and A. L. Geary, J. Electrochem. Soc. **104**, 56 (1957).

44. J. Schindelin, I. Arganda-Carreras, E. Frise, V. Kaynig, M. Longair, T. Pietzsch, S. Preibisch, C. Rueden, S. Saalfeld, B. Schmid, J. Y. Tinevez, D. J. White, V. Hartenstein, K. Eliceiri, P. Tomancak, and A. Cardona, Nat. Methods **9**, 676 (2012).

45. G. Chao, D. Kuhlmann-Wilsdorf, and D. D. Makel, Wear **162**, 1139 (1993).

46. S. H. Jeong, S. J. Yong, and Y. Z. Lee, Tribol. Trans. **50**, 564 (2007).

47. A. Zafari, H. M. Ghasemi, and R. Mahmudi, Wear **292**–**293**, 33 (2012).

48. F. Labib, H. M. Ghasemi, and R. Mahmudi, Wear **348**–**349**, 69 (2016).

49. J. F. Archard and W. Hirst, Proc. R. Soc. London. A. Math. Phys. Sci. **236**, (1956).

50. M. Pole, M. Sadeghilaridjani, J. Shittu, C. Mahajan, N. Ghodki, and S. Mukherjee, Mater. Sci. Eng. A **816**, 141315 (2021).

51. E. Hornbogen, Wear **33**, 251 (1975).

52. M. Kobayashi, Y. Zhang, H. Ishikawa, J. Sun, J. Oddershede, D. Juul Jensen, and H. Miura, Exp. Mech. 1 (2021).

53. A. Pola, M. Tocci, and F. E. Goodwin, Metals (Basel). **10**, 1 (2020).

54. GrantaDesign (https://www.azom.com/properties.aspx?ArticleID=749).

55. N. N. Aung, W. Zhou, and L. E. N. Lim, Wear **265**, 780 (2008).

56. Y. Meng, L. Liu, D. Zhang, C. Dong, Y. Yan, A. A. Volinsky, and L. Wang, Bioact. Mater. **4**, 87 (2020).

57. G. Williams, C. Kousis, N. McMurray, and P. Keil, Npj Mater. Degrad. **3**, (2019).

58. S. Song, G.-L. Song, W. Shen, and M. Liu, Corrosion **68**, 15005 (2012).

59. G. Williams and R. Grace, Electrochim. Acta **56**, 1894 (2011).

60. C. Kousis, P. Keil, H. N. McMurray, and G. Williams, Corros. Sci. **206**, 110477 (2022).

61. L. Wang, Y. Peng, T. Nakata, C. Xu, J. Sun, Z. Zheng, Y. Li, F. Cao, L. Geng, and S. Kamado, Corros. Sci. **255**, 113151 (2025).

62. P. N. Myagkikh, E. D. Merson, V. A. Poluyanov, and D. L. Merson, Lett. Mater. **15**, 55 (2025).

63. C. Xie, H. Li, X. Zhou, and C. Sun, Surf. Coatings Technol. **374**, 797 (2019).